Journal of Applied Physics ARTICLE pubs.aip.org/aip/jap

Optimizing laser-induced phase transformations in Sb_2S_3 thin films: Simulation framework and experiments

Cite as: J. Appl. Phys. **136**, 173108 (2024); doi: 10.1063/5.0224152
Submitted: 19 June 2024 · Accepted: 21 October 2024 ·
Published Online: 5 November 2024

J. Resl,[1,a)] K. Hingerl,[1] Y. Gutierrez,[2] M. Losurdo,[3] and C. Cobet[1]

AFFILIATIONS

[1]Johannes Kepler Universität, Altenberger Straße 69, 4040 Linz, Austria
[2]Departamento de Física Aplicada, Universidad de Cantabria, Avenida de los Castros, s/n, Santander 39005, Spain
[3]Istituto di Chimica della Materia Condensata e delle Tecnologie per l'Energia, ICMATE, CNR, C.so Stati Uniti 4, Padova 35127, Italy

[a)]**Author to whom correspondence should be addressed:** josef.resl@jku.at

ABSTRACT

We present a novel simulation approach combined with pulsed laser experiments, spectroscopic ellipsometry, and Raman spectroscopy to comprehensively analyze phase transformation dynamics in thin films. The simulations apply to any thin film stack and incorporate critical factors, such as thin film interference, heat transfer, and temperature-dependent optical properties during heating and melting. As a case study, we investigate the picosecond laser-induced amorphization of antimony sulfide (Sb_2S_3) thin films, a promising alternative to traditional phase-change materials in photonic applications to validate the simulation model. The computational efficiency of our simulations enables not only the investigation of the laser-induced phase transformation but also the optimization of key process parameters and parameter fitting. The simulations identified optimal film thickness and laser fluence parameters that maximize energy efficiency, melting effectiveness, and quenching rate while ensuring high reflectivity contrast between the amorphous and crystalline states. By constructing a wide-ranging, high-resolution parameter map of the laser fluence and film thickness dependence of the melting process, we demonstrate how this model guides the understanding of phase transformation dynamics. Raman spectroscopy confirms the polycrystalline to amorphous transition of Sb_2S_3 and provides a semiquantitative estimate of the amorphous fraction as a function of laser fluence, which is qualitatively consistent with the simulation predictions of the model. The open-source simulation framework, experimentally validated, provides valuable insights into laser-induced amorphization dynamics in Sb_2S_3 and related phase-change material thin films, enabling rapid optimization of photonic devices.

INTRODUCTION

In recent years, many phase-change materials (PCMs) have been explored.[1] These materials aim to rival the properties of the GeSbTe-family (GST) by offering comparable performance in some respects while expanding the scope of applications. PCMs offer drastically different optical and electrical properties in the (poly)crystalline and amorphous states. This makes PCMs very attractive in many novel photonic devices like tunable all-dielectric metasurfaces,[2–5] polarization, and band-sensitive photodetectors,[6,7] reconfigurable optical switches,[8] switchable color pixels,[9] and a wide variety of on-chip photonic components.[10–12] Competing chalcogenide material systems from the V–VI or III–VI semiconductor groups are currently under strong investigation, such as Sb_2S_3[13–15] used in our experiments, as well as Sb_2Te_3,[1] Bi_2Te_3,[16] and GaS.[17] Each of these materials has its unique characteristics and depending on the method of deposition[18,19] and the postprocessing parameters the optical and thermal properties differ due to variations in microstructure.[20]

Controlling the local and reversible phase transformation in Sb_2S_3 is of major importance for future applications, and an appealing method for amorphization is to exploit laser pulses.[21] For the amorphous-to-crystalline phase transformation and vice versa, key parameters are the optical energy needed per volume of material or area of film to enable the transformation or the heating

time/cooling rate needed to enable/prevent crystallization. Many publications do not consider these key parameters, and often it is not possible to infer them from the experimental parameters that are given.

In this contribution, we aim for a better comparison of different PCMs and different deposition methods, concerning amorphization energy density as well as the critical cooling rate and the overall dynamics of the amorphization process. This process involves the melting of a crystalline solid, followed by fast cooling (quenching) of the melt. The quenching is performed above the critical cooling rate, so that no recrystallization occurs, and a glassy, disordered state is achieved. From a thermodynamic perspective, this transformation is a non-equilibrium transition. Many laser heating simulations from literature neglect either interference,[22] melting,[23] or the change of optical properties during melting or a combination of thereof.[24] A similar study[21] focuses in contrast to our study on much longer pulse durations and does not examine time-dependent heating dynamics or mixed-phase regions. In this study, we conduct simulations and experiments. We developed an appropriate mathematical model and implemented it as a Python script to enable fast and open-source simulations.[25] This has four key benefits. First, we gain a better understanding of the amorphization process through modeling. Second, this model enables us to predict the outcomes of state-of-the-art experiments, thereby reducing the necessity for extensively exploring a complex, multi-parameter experimental space. Third, the simulations run in seconds, allowing us to fit less known parameters, like the PCM melt's absorption coefficient, to experimental data if the simulation results qualitatively match. Last, we can use the simulations to optimize any figure of merit like the cooling rate or the heating efficiency of the laser amorphization process.

We consider several factors that influence the heating and melting of a thin film with a laser. Our simulations incorporate the most important parameters, such as the laser intensity and pulse duration, as well as the thermal and optical properties of the thin film and substrate. Furthermore, we include important effects like thin film interference, heat conduction, change of optical properties upon heating and melting, and cooling after the laser pulse.

To validate the model, we have carried out laser amorphization experiments on antimony sulfide PCM (Sb_2S_3) thin films to compare with our simulations and to study Sb_2S_3 material properties and phase transformation dynamics. This is of particular interest, as Sb_2S_3 is a highly researched and relevant PCM, that has been used and integrated into a wide range of different devices, such as on-chip components[10,14,26,27] and metasurfaces.[2,5]

This paper presents the physical models in the theory section, followed by simulation details, parameters as well as the simulation results. The experimental section describes the laser amorphization process and results. The discussion section examines key principles of the laser amorphization process and compares the simulation and experimental findings.

MODEL FOR LASER MELTING IN THIN FILMS

To accurately model the laser heating process (Fig. 1) in space (x, y, z coordinates) and time t, we must consider the interplay between the temperature distribution $T(x, y, z, t)$ and the distribution

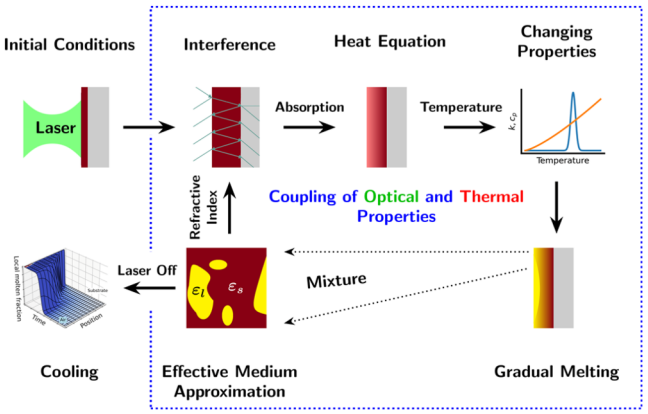

FIG. 1. General dynamics of the picosecond laser amorphization of thin films.

of the electric field $\mathbf{E}(x, y, z, t) = \{E_x(x, y, z, t), E_y(x, y, z, t), E_z(x, y, z, t)\}$ mediated via key physical phenomena. These phenomena include the interference and absorption of the laser light within the thin film, as well as the resulting localized heating and conduction of heat. Additionally, we must account for temperature-induced changes in material properties, such as the absorption coefficient, specific heat capacity, and changes due to melting.

The overall dynamics of the laser heating process are as follows: once the laser pulse arrives, the electric field $\mathbf{E}(x, y, z, t)$ of the laser pulse interacts with the material. The absorbed power per volume in the film is

$$p = \alpha \frac{1}{2} \varepsilon_0 \, c \, n |\mathbf{E}|^2 = \alpha |\mathbf{S}|, \tag{1}$$

where $\alpha(T)$ is the temperature-dependent absorption coefficient, ε_0 denotes the vacuum permittivity, c is the speed of light, n is the real part of the refractive index, and $\mathbf{S}$ is the Poynting vector. The absorption in the thin film depends on the local electric field distribution and local absorption coefficient. The local electric field is determined by laser intensity and the refractive indices and the film thicknesses of the thin film stack. Once the temperature starts to rise with absorption, the thermal properties like heat capacity $c_p(T)$ and optical properties $n(T)$, $\alpha(T)$ of the thin film begin to change. To account for this coupled problem, at each timestep, the electric field distribution within the film (interference), heating, and heat conduction must be calculated.

Model assumptions

The design of both the simulations and experiments is focused on facilitating rapid heating, melting, and quenching to study the key processes involved in the amorphization of thin films and to enable rapid optical switching. This has guided the selection of laser parameters.

We selected a pulse duration in the picosecond range (30–35 ps), as heating of the crystal lattice in solids occurs on a comparable or longer timescale. The rate at which the crystal lattice can be heated is fundamentally limited by the phonon frequencies, with an oscillation period of 100–200 fs [estimated from Raman spectra in Fig. 7(c) for peaks between 300 and 150 cm^{-1}] in Sb_2S_3 for optical phonons. More important is the strength of electron–phonon coupling, which generally pushes the timescale of lattice heating into the single-digit picosecond range.[28,29] As a result, even if the laser energy is transferred to the electrons almost instantaneously, the lattice heating will occur on a time scale much longer than the phonon frequencies.

If the pulse duration extends up to tens of nanoseconds, the cooling rate would be limited by the already ongoing heat conduction to the surrounding volume. These pulses would then be too long for amorphization. To be specific, through heat conduction from the heated thin film into the depth of the substrate, a much larger volume than the region of the thin film, which is targeted with the laser beam is heated. This heating depth can be quantified by the thermal diffusion length $L = \sqrt{4\,a\,\tau_p}$. Here, a is the thermal diffusivity of the substrate and τ_p is the laser pulse duration. This results in a thermal diffusion length of 3.2 μm for silicon at room temperature with a pulse duration τ_p of 30 ns and the thermal diffusivity of Si of $a = 87\ mm^2/s$.[30] Such a large, heated volume severely limits the achievable cooling rate because a larger heated region cools much slower due to lower temperature gradients. So, when using nanosecond pulses with just enough pulse energy to achieve full melting, the heating process would be slow, and the cooling process would be even slower.

Our simulation method is very general and can be used with any type and number of thin films or laser parameters, which fulfill the following criteria: We assume for the optical part of the simulation that the plane wave approximation is valid. This means a large beam diameter compared to the thickness of the film stack and a low beam divergence angle. This first criterion is easy to fulfill, as a typical laser spot is larger than half of its wavelength, even when strongly focused. Furthermore, since we are working in the visible range and require a low beam divergence, the spot size will be much larger than the wavelength. In addition, the pulse duration should be long enough (1 ps or more), such that the wavelength of the pulse is well-defined for calculating thin film interference.

Thin film interference

In a planar layered structure, the reflection, transmission, and absorption of light are strongly dependent on the properties of the stacked layers. The coherent superposition of the light waves resulting from multiple reflections within the layers determines the overall optical response of the sample. The relative phase of these waves depends on the thickness of the films, the angle of incidence, the refractive indices of the layers, and the wavelength of the light.

The Abelès matrix formalism[31,32] can be used to calculate the complex electric fields (amplitude and phase) of the forward and backward traveling waves in homogeneous materials. This formalism allows for the determination of the electric field at each depth within the layered structure. Each layer can be further divided into an arbitrary number of sublayers, with the formalism applied to each

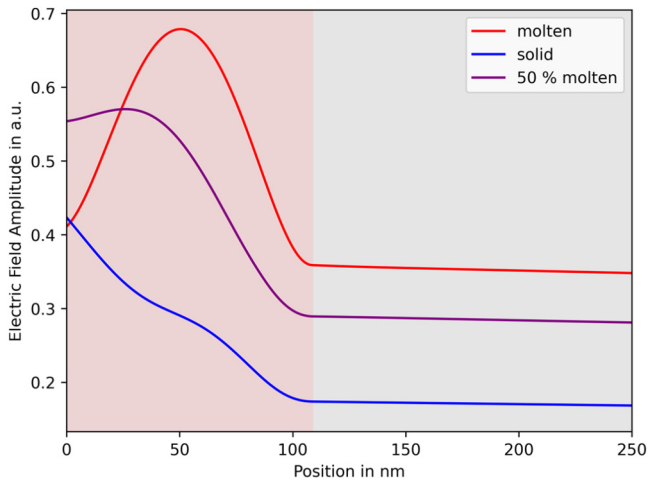

FIG. 2. Electric field amplitude distribution during the melting process of a 109 nm thick film [depicted in Fig. 5(b)]. As the film melts, the maximum electric field amplitude shifts from the top surface (zero position) toward the center of the film. The film melts from the top surface down toward the substrate (shown in gray).

sublayer. This is particularly important when the optical properties of the film change locally across the thickness with temperature or even when a phase transition like melting occurs. This also enables the calculation of local absorption. The absorbed power per volume can be calculated using the local electric field distribution and the absorption coefficient of the materials [see Eq. (1)].

Figure 2 illustrates how the electric field distribution evolves during the melting process for a 109 nm thick Sb_2S_3 film, corresponding to the simulation in Fig. 5(b). As the film progressively melts from the top surface toward the substrate, there is a substantial change in the electric field profile. In the solid state, represented by the blue curve, the maximum electric field amplitude is located at the top surface of the film. However, as the film melts, as shown by the purple curve, this maximum shifts toward the center of the film. When fully molten, as depicted by the red curve, the maximum electric field amplitude is located at the center of the film. Concurrently, the amplitude of the electric field increases significantly. This increased amplitude directly impacts the absorbed power density. The altered electric field distribution is a consequence of the change in refractive index and absorption coefficient between the solid and molten states of Sb_2S_3. This simulation reveals the profound effect of melting on the film's optical properties and electric field profile, significantly altering local laser absorption during melting.

Heating, heat conduction, and melting

The heat introduced locally by the laser absorption starts to spread through the material. We use a one-dimensional (1D) model for heat conduction in this study, which is justified by several key factors. The volume of the heated region is primarily

confined to the thin film, as the substrate is much less absorbing. Due to the short pulse duration (less than 1 ns), the heat diffusion length is minimal, causing the heated region to closely coincide with the absorption region during the heating phase and most of the cooling phase. This results in a very thin heated layer. The large laser beam diameter ensures uniform heating across the plane of the film, leading to extremely small in-plane temperature gradients $\vec{\nabla}_{x,y}T$ and consequently negligible in-plane heat flow $\vec{q}_{x,y}$,

$$\vec{q} = \vec{q}_{x,y} + \vec{q}_z \propto -\vec{\nabla}_{x,y}T - \vec{\nabla}_z T \approx -\frac{\partial T}{\partial z}\,\hat{z}, \tag{2}$$

with $|\vec{\nabla}_z T| \gg |\vec{\nabla}_{x,y}T|$.

Here, $\vec{q}$ is the heat flow, with in-plane components $\vec{q}_{x,y}$ and normal component $\vec{q}_z$. The in-plane component of the temperature gradient is $\vec{\nabla}_{x,y}T$ and the normal component is $\vec{\nabla}_z T$, while $\hat{z}$ is the unit vector in z direction.

So, the largest temperature gradient is $\vec{\nabla}_z T$ and occurs normal to the layer, into the depth of the material. Given these conditions, the in-plane dimension can be safely neglected, and a 1D model focusing on heat conduction perpendicular to the film surface is sufficient. Moreover, radiative heat transfer can be neglected in comparison to heat conduction, as will be shown later in a brief estimation. Consequently, the 1D heat equation suffices,

$$\frac{\partial T}{\partial t} = a\left(\frac{\partial^2 T}{\partial z^2}\right) + s(z), \tag{3}$$

with $a = \frac{l}{\rho\, c_p}$ and $s(z,t) = \frac{p(z,t)}{\rho\, c_p}$ for each layer.

Here, a is the thermal diffusivity, z is the position on the axis, which is normal to the thin film plane, $s(z)$ is the power density everywhere in the stack, l is the thermal conductivity, ρ is the mass density, c_p is the specific heat capacity at constant pressure, and $p(z,t)$ is the absorbed power per volume in space and time as defined in Eq. (1).

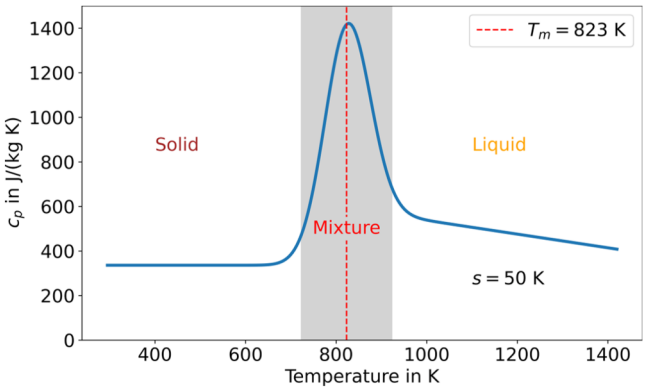

FIG. 3. Smoothed heat capacity with specific heat of melting.

Melting

As the laser energy is absorbed and the temperature rises, the material begins to melt once it reaches its melting point. We model melting by including the specific heat of melting h_m in the specific heat capacity of the material,

$$c_p(T) = \begin{pmatrix} c_{\mathrm{s},0} + T c_{\mathrm{s},T} & \text{for} & T \le T_\mathrm{m} \\ c_{\mathrm{l},0} + T c_{\mathrm{l},T} & \text{for} & T > T_\mathrm{m} \end{pmatrix} + h_\mathrm{m}\delta(T - T_\mathrm{m})\,. \tag{4}$$

The specific heat capacity shows a linear temperature dependence for the solid and the liquid phase. The constants $c_{\mathrm{s},0}$ and $c_{\mathrm{l},0}$ are the temperature independent components of the specific heat capacity in the solid and the liquid phase, while $c_{s,T}$ and $c_{l,T}$ are the linear temperature coefficients. The melting temperature is T_m and δ is the Dirac delta distribution. To make the solution obtainable with an acceptable number of timesteps in a numerical implementation, a melting interval of several Kelvins is used to smooth the hard discontinuity of $\delta(T - T_\mathrm{m})$. We smooth the full heat capacity in Eq. (4) by convolving it with a Gaussian distribution of standard deviation s,

$$c_{p,\,\mathrm{smoothed}}(T) = \frac{1}{2}\left((c_{\mathrm{l},0} + T c_{\mathrm{l},T})\left(\mathrm{erf}\left(\frac{T - T_\mathrm{m}}{\sqrt{2}s}\right) + 1\right) + (c_{\mathrm{s},0} + T c_{\mathrm{s},T})\,\mathrm{erfc}\left(\frac{T - T_\mathrm{m}}{\sqrt{2}s}\right)\right) + \frac{e^{-\frac{(T-T_\mathrm{m})^2}{2s^2}}(s^2(c_{\mathrm{l},T} - c_{\mathrm{s},T}) + h_\mathrm{m})}{\sqrt{2\pi}s}. \tag{5}$$

This formula is generally applicable to all materials with a linear temperature dependence of c_p and is plotted in Fig. 3 for Sb_2S_3.

When a PCM melts, the optical properties change drastically. In contrast to slower heating[21] with longer pulses, for fast heating in the low digit picosecond range (30–35 ps), heat conduction is slow, such that a mixed-phase region forms, where the temperature is close to the melting point. In this region, the material is semi-molten, with solid and liquid domains (see Fig. 1). Then, the PCM layer's optical properties, described by its effective dielectric function ε_eff, are a nonlinear combination of the solid ε_s and liquid ε_l phases due to screening effects. The Bruggeman effective medium approximation[33] is widely used to account for this in mixtures with similar volume fractions,

$$f_\mathrm{s}\frac{\varepsilon_\mathrm{s} - \varepsilon_\mathrm{eff}}{\varepsilon_\mathrm{s} + 2\varepsilon_\mathrm{eff}} + f_\mathrm{l}\frac{\varepsilon_\mathrm{l} - \varepsilon_\mathrm{eff}}{\varepsilon_\mathrm{l} + 2\varepsilon_\mathrm{eff}} = 0. \tag{6}$$

The equation can be solved in closed form if both volume fractions added together are 1,

$$\varepsilon_{\text{eff}} = \frac{1}{4}\left(\sqrt{8\varepsilon_s\varepsilon_l + ((3f_s - 2)\varepsilon_l + \varepsilon_s(1 - 3f_s))^2} + (2 - 3f_s)\varepsilon_l + \varepsilon_s(3f_s - 1)\right). \quad (7)$$

We use ε_{eff} to calculate the effective refractive index n_{eff} and the effective extinction coefficient k_{eff}, which we use then for the thin film interference calculation and in Eq. (1). Starting from Eq. (5), the local molten fraction f_l can be calculated for each temperature at every point in the film with the following formula, provided that the temperature $T(z, t)$ is known through solving the heat equation through simulation [we use the finite element method (FEM)],

$$f_l(z, t) = f_l(T(z, t)) = \frac{1 + \text{erf}\left(\frac{T(z, t) - T_m}{\sqrt{2}\, s}\right)}{2}. \quad (8)$$

Simulation details and parameters

Simulation workflow

Our simulation workflow can be seen in Fig. 1. The most important aspect of our laser heating simulations is that the material parameters are temperature dependent. This couples the wave equation for the electric field with the heat equation. To efficiently solve both equations simultaneously, we employ the Abeles transfer matrix algorithm, the finite element method (FEM), and an iterative forward-stepping method, which is very effective due to the well-behaved (smoothness) of the temperature dependence of the material properties in our model. One timestep works like this: First, the absorbed power is calculated via interference and the power is used to calculate the temperature increase and the heat conduction. With the calculated temperature, the thermal and optical properties are recalculated for the next time step.

Spatial and temporal parameters

The simulations were carried out with a laser pulse duration τ_p of 33 ps at a wavelength λ of 532 nm at normal incidence. This pulse duration ensures rapid heating that is localized in the film. The chosen wavelength leads to moderate absorption for crystalline Sb_2S_3 with an absorption coefficient of 0.015 nm^{-1} at the laser wavelength and a corresponding optical penetration depth of 65 nm in the film, which both have been calculated from the refractive index given in the section titled "Material parameters." This penetration depth is comparable to the film thickness of 109 nm and is a balance between two extremes. On one hand, high absorption results in high absorption efficiency, but only the topmost part of the film is heated, as the penetration depth is much lower than the film thickness (at a wavelength of 300 nm the penetration depth would be approximately 10 nm). On the other hand, low absorption allows light to penetrate and heat the whole film, as the penetration depth is much larger than the film thickness, but the overall heating efficiency is low (at a wavelength of 700 nm the penetration depth is approximately 1000 nm). The laser pulse is modeled with a binary temporal profile, with a fixed intensity when switched on and zero intensity when switched off.

The overall simulation time is the length of the laser pulse of τ_p, which only includes the heating phase of the process. By simply extending the simulation time, cooling can be simulated too. The simulation time step was chosen as 0.05 ps. The spatial resolution for the thermal simulation was 0.5 nm, with the simulation domain encompassing the whole thin film (9–250 nm thickness) and 400 nm of substrate. For the cooling simulation, the substrate domain has been extended to exclude boundary effects. For the optical simulation, the domain was sliced into layers of also 0.5 nm, such that each grid point in the thermal simulation was represented by its own layer for the simulation of interference and absorption. The surface of the sample was taken as perfectly insulating with no heat flux because thermal radiation and heat conduction to air are negligible at this timescale. Thermal radiation can be estimated with the Stefan–Boltzmann law and is of the order of nanowatts per square micrometer. This is around 7 orders of magnitude less than the laser power. On the substrate side, the boundary condition is not critical, when enough of the substrate is simulated. It can be taken either as constant at room temperature of 22 °C, perfectly insulating, which is our choice, or as a "natural" boundary condition that allows for a much smaller simulation domain by reducing boundary effects. More details on the natural boundary condition can be found in the supplementary material.

Material parameters

For Sb_2S_3, the temperature-dependent heat capacity, the melting temperature of 823 K, and the latent heat of melting were taken from the literature.[34] The temperature dependence of the heat capacity in the solid state is negligible[34] and Eq. (4) for the specific heat capacity in J/(kg K) is then

$$c_p(T) = \begin{pmatrix} 336 & \text{for} & T \le 823\ \text{K} \\ 844 - 0.307035\ T & \text{for} & T > 823\ \text{K} \end{pmatrix} + 120223\ \delta(T - 823\ \text{K}). \quad (9)$$

For the smoothing of the heat capacity, $s = 20$ K was used. This rather large value was taken for numerical convenience, because it speeds up the simulations, with minimal influence on the final local molten fraction of the film. The heat conductivity was set to 0.216 W/(m^2 K).[35] This is the value for the amorphous phase, and it was applied to the crystalline and liquid phases as well, because the introduced error is negligible, as there is almost no heat conduction during the duration of the laser pulse. However, heat conduction is very important during the cooling of the amorphous phase. For the mass density, an average value of 4380 kg/m^3 was taken.[36] The refractive index for the polycrystalline phase at the laser wavelength was taken as 3.77 + i 0.654 with no temperature

dependence. The value has been derived from spectroscopic ellipsometric analysis of our samples and the wavelength dependence can be seen in Fig. 4. Specifically, post-annealing measurements at room temperature were performed on films with different thicknesses. A combined multi-sample fit using a Tauc–Lorentz oscillator model was performed to extract the optical properties. From that, we calculate an absorption coefficient of 0.015 nm^{-1} at the laser wavelength and an optical penetration depth of 65 nm. We neglected the temperature dependence of the optical properties for two reasons. Below 573 K, this dependence was weak. Above 573 K, the slow heating process (compared to the timescale of the laser pulses) led to film deterioration, preventing measurement via *in situ* spectroscopic ellipsometry. The refractive index of the molten Sb_2S_3 film was taken as 2.33 + i 0.0479 because we assumed that the molten Sb_2S_3 film's refractive index matches that of the as-grown amorphous Sb_2S_3 films. This is a simplification due to the porous nature of the amorphous film produced by chemical bath deposition. To characterize the amorphous phase, we performed measurements on several as-deposited films with different thicknesses. A multi-sample fit using a Cody–Lorentz oscillator model was used to extract the optical properties. However, this reasonable hypothesis, based on the similarity between the disordered liquid and amorphous states, proved quite useful in the absence of specific data. With that, we calculate an absorption coefficient of 0.0011 nm^{-1} at the laser wavelength and an optical penetration depth of 884 nm for the liquid phase.

The material parameters of silicon are well known. We kept them fixed at their room temperature values. Only the dielectric function was used in a temperature-dependent form. Specific values were taken from the materials library of the CompleteEASE 6 software[37] and fitted with a polynomial for the wavelength of 532 nm,

$$\varepsilon(T\,\text{in}\,^\circ\text{C}) = (17.1 + 3.5\times10^{-3}\,T + 1.75\times10^{-6}\,T^2) + \text{i}(0.174 + 9.51\times10^{-4}\,T + 4.72\times10^{-6}\,T^2). \quad (10)$$

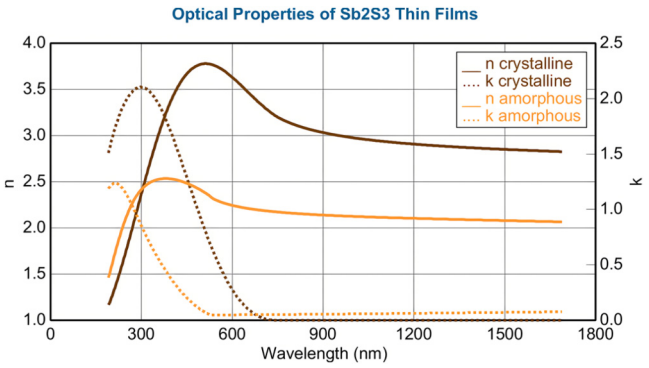

FIG. 4. Refractive index and extinction coefficient of amorphous and thermally crystallized Sb_2S_3 thin films determined with spectroscopic ellipsometry. The crystalline film shows a higher refractive index *n*, a higher extinction coefficient *k*, and a red-shifted absorption edge compared to the amorphous film. The absorption onset shifts from 528 nm in the amorphous film to 743 nm in the crystalline film.

Simulation results

We created a wide-ranging, high-resolution parameter map [Fig. 5(a)] that provided an overview of the laser melting process. The map was constructed by running a unique simulation for each combination of selected film thicknesses and laser fluences. Figure 5(a) displays the average molten fraction, which is the average of the local molten fraction across the film, as a function of laser fluence *F* and film thickness. For this map, *s* for the smoothing of the heat capacity has been set to 50 K to increase the speed of the simulation. The onset of melting occurs at approximately 10 mJ/cm^2 for a 109 nm thick film with 5% of the film becoming molten, which we later will compare to our experiments. As the laser fluence increases above 50 mJ/cm^2, the melting saturates. The average molten fraction rises the most with increasing laser fluence for films around 50 nm thick, corresponding to the most pronounced maximum of the film thickness oscillations. This maximum shifts to higher film thicknesses as the film progressively melts. Very thin films of 30 nm or less require higher laser fluence to melt because the substrate cools the film significantly and the film exhibits a high reflectivity.

In our simulations, the heating process [Fig. 5(b)] of a 109 nm thick film happened as follows: the film was heated and melted from front to back (substrate side) and achieved melting quite early on (around 2 ps) during the laser pulse, then the heating and melting slowed. Notable are oscillations in the temperature curves, which occurred in the solid phase with a smaller wavelength and a much lower amplitude than in the liquid phase. This was due to the change in the effective refractive index and extinction coefficient between the solid and liquid phases. As a result, the interference and distribution of the amplitude of the electric field were modified (see Fig. 2). First, the maximum of the electric field was at the top of the film and when the film melted, the maximum shifted to the center of the film. Also, the substrate heated to some degree, and a minor fraction of the film near the substrate stayed solid due to the heat conduction of the substrate. The substrate heating was more pronounced, when the film was molten, due to an increased electric field amplitude (see Fig. 2). A simulation of a thicker film with twice the thickness is shown in Fig. 5(d). The temperature profiles were markedly different. Melting also proceeded from front to back. It took similar times to achieve full melting (~10 ps). The final temperature profile at the end of the pulse exhibited two maxima.

In Fig. 5(c), the local molten fraction of the thin film after laser irradiation has been simulated. Initially, the film is almost fully molten, except for a very thin slice adjacent to the substrate. The cooling process is very much non-uniform in the film and extremely rapid, with a cooling rate exceeding 7 K/ns. The film solidifies first near the substrate interface due to rapid heat conduction to the adjacent substrate, while the surface remains molten for a much longer period because the distance to the substrate is larger and the heat transport to the air is negligible. Important is the timescale of solidification of approximately 65 ns. The dark blue color indicates points in space and time with a cooling rate greater than 7 K/ns, which was sufficient to suppress crystallization in the experiments. This high-cooling-rate region encompasses the entire solidification region, ensuring that the material remains amorphous throughout the process.

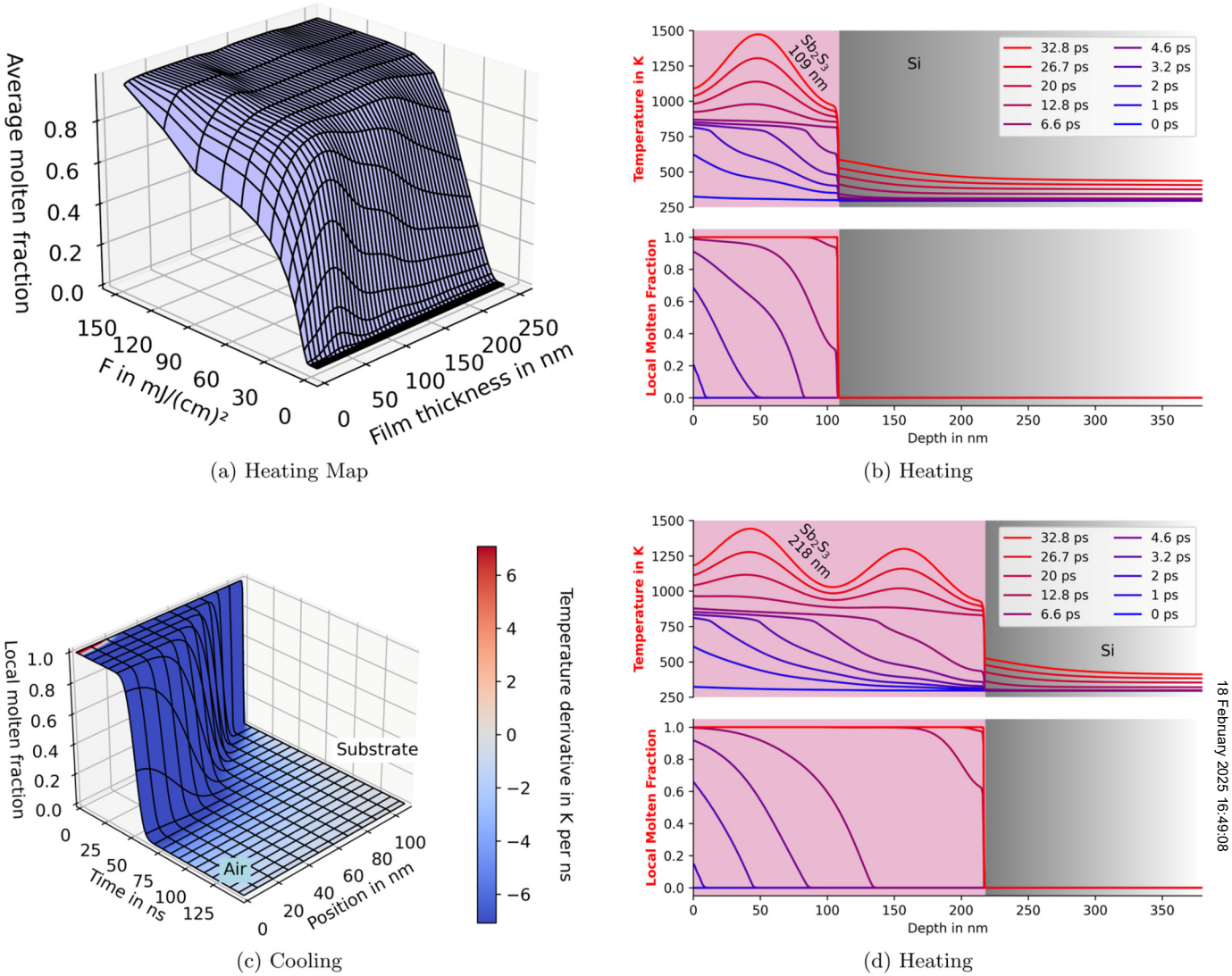

FIG. 5. Simulation results for: (a) Parameter map of the average molten fraction of the whole Sb_2S_3 thin film at the end of the laser pulse as a function of laser fluence F and film thickness. (b) Time evolution of temperature (top panel) and local molten fraction (bottom panel) within a 109 nm thick, thin film of crystalline Sb_2S_3 and Si substrate during laser irradiation (pulse starts at 0 ps and ends at 33 ps). Each curve represents a different time instant during the laser pulse. The laser fluence was 139 mJ/cm^2 in this simulation. (c) Time evolution of the local molten fraction within the 109 nm Sb_2S_3 thin film after the end of the laser heating [see (b), the end of the pulse is set to $t = 0$ ns]. A value 1 means fully molten, while 0 is solid (amorphous or crystalline). The silicon substrate is not shown. The time derivative of the temperature is indicated by the color of the plot, where red is heating, and blue is cooling. The dark blue color indicates a cooling rate greater than 7 K/ns. (d) Simulation of a film twice as thick (218 nm) as in (b) and everything else unchanged.

EXPERIMENTS

Experimental details

Laser amorphization

We used a laser wavelength of 532 nm in our experiments, with a pulse duration of 30–35 ps with a box shape in time. The pulse energy was 39.6 μJ and measured with a Coherent® LabMax-TOP with an energy detector. The sample was irradiated with a weakly focused beam with a low beam spreading angle of 1.7° of the FWHM (full width at half maximum) and relatively large spot diameters, which were measured with the knife's edge method. The sample was placed on top of three stacked single-axis translation stages to create a rectangular raster of laser-treated spots [see Fig. 6(c)]. This enables the exploration of a large parameter space in a single, well-controlled experiment. The experiments

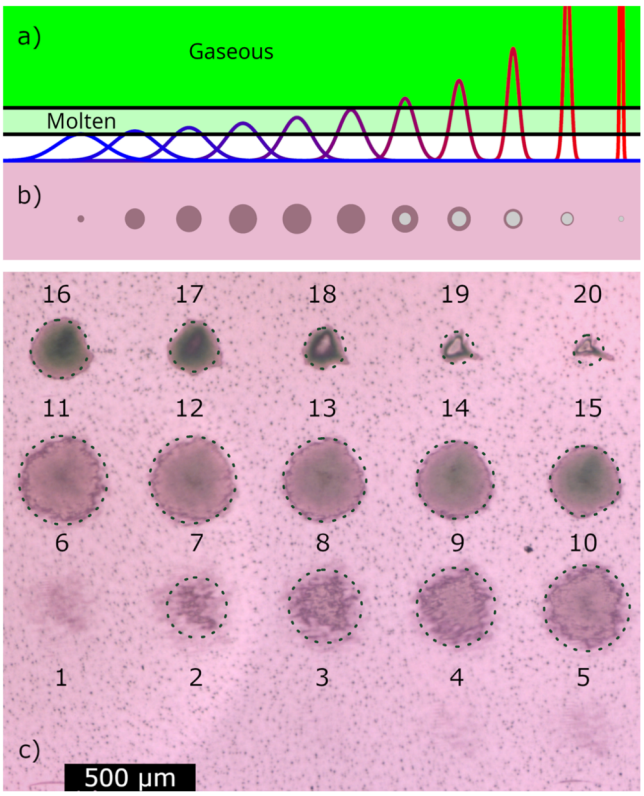

FIG. 6. (a) Schematic of the laser fluence distribution of a beam as it gets focused on the sample from the left to the right, with melting and evaporation thresholds indicated as lines and the molten phase shaded in light green and the gas phase in green. (b) Associated changes on the sample when viewed from the top. Pinkish is crystalline, darker is amorphous, and gray is ablated. (c) Stitched microscopy image showing a raster of laser-treated spots on the thin film with increasing laser fluence from bottom to top and from left to right, with spot index indicated. The dashed circles indicate the spot size determined in Fig. 7(a) using Eq. (11). The lighter color of the background on the lower left side is a stitching artifact.

were carried out in air and at room temperature. The creation of the raster was performed in the following way: The focus of the laser beam was above the sample surface and for each spot in the raster, all laser parameters were kept the same. After each laser "shot," the sample was lifted by 1 mm upward toward the focus region to decrease the spot size and, therefore, increase the energy per area, hence the fluence of the laser on the sample surface. The focus region itself was never reached and always above the sample. For each spot, the sample was at rest and one single laser pulse was applied to the surface of the film.

The distance between rows and columns in the raster is 500 μm, the FWHM of the laser spot was between 617 and 54 μm and was decreased by 29.6 μm per mm when stepping the sample upward through a range of 20 mm to irradiate at 20 different laser fluences.

Sample preparation, processing, and characterization

All procedures were carried out in air at room temperature unless otherwise stated. Amorphous antimony trisulfide (Sb_2S_3) thin films have been deposited by chemical bath deposition following a low-temperature recipe.[38,39] The amorphous Sb_2S_3 thin films were grown on a silicon (100) substrate. This substrate was chosen because it has well-defined optical and thermal properties and is stable at elevated temperatures. In addition, the high thermal conductivity supports the amorphization process. The deposition temperature of the chemical bath was 7 °C and the deposition time was 110 min to obtain a film thickness of 183 nm. The samples were first rinsed with ultrapure water and dried using N_2 blowing after deposition. They were then measured by spectroscopic ellipsometry to determine optical properties and film thicknesses by fitting a Cody–Lorenz oscillator model to the data. Subsequently, the samples were immediately stored in a glovebox under N_2 atmosphere. This atmosphere maintained less than 0.5 ppm of oxygen and water, essential to prevent any possible sample deterioration.

The amorphous samples were then crystallized by thermal annealing, which was performed inside an enclosed heating cell (Linkam THMSEL600) connected to a spectroscopic ellipsometer (Wollam M-2000 UV-VASE) for spectroscopic ellipsometry measurements of the optical properties. The procedure was as follows: First, the sample was measured by spectroscopic ellipsometry at room temperature at multiple angles of incidence. Then, the cell was purged for at least 10 min with a flow of argon 5.0 to remove humidity and oxygen in the cell. Afterward, the sample was heated at a rate of 25 °C/min up to 265°C to induce crystallization. During heating, real-time spectroscopic ellipsometry measurements were recorded at an incidence angle of 70°. The temperature of 265 °C was held for at least 35 min while the ellipsometric transients stabilized. This ensures that no further optical change is happening and that the crystallization process is completed. Afterward, the temperature was ramped down with the same rate of 25 °C/min and after opening the cell, the sample was measured at multiple angles of incidence again. The sample thickness was reduced from 183 to 109 nm during crystallization.

For Raman spectroscopy, a Horiba LabRam Aramis VIS Raman spectrometer was used. The Raman laser excitation wavelength was 532 nm in a backscattering configuration with a 50× microscope objective. The laser power applied to the sample surface was 5 mW with a spot diameter of 2.6 μm. The laser was linearly polarized, while no specific polarization was applied to the Raman signal collection. Measurements were taken with an acquisition time of 15 s and two accumulations (averaging of 2 spectra), allowing for a sufficient signal-to-noise ratio.

Experimental results

In our experiments, we analyzed the structural changes in Sb_2S_3 thin films induced by picosecond laser treatment with optical microscopy and Raman spectroscopy to check the validity of the simulations. The thickness of the film is 109 nm, which was also used in the simulations to allow comparison to the experiments.

Figure 6(c) displays the outcomes of laser treatment on a crystalline Sb_2S_3 sample. Figures 6(a) and 6(b) provide a schematic illustration of how the treated area is expected to change as the

laser spot size varies. The sample colors described here are as they appeared under the microscope. These colors vary with lighting conditions due to thin film interference. As the laser spot size decreased, the sample initially appeared unaltered (spots 1–4), then the treated area on the sample increased (spots 5–11), followed by a subsequent decrease (spots 12–20).

When moving from the outer edge of the laser-treated areas toward their respective center, the sample underwent a series of changes as the applied laser fluence increased. The first change is a diffuse shadow (spot 6), which transitioned to a darker color (spot 7). As the laser spot size further decreased, the color became lighter again (spot 9), followed by a gradual shift to green (11–15). For spots 16–20, continuing toward the center of the laser spot, the color changed to black and finally to gray.

An analysis of the outer radii of the spots to estimate the onset of film modification can be seen in Fig. 7(a). For fitting the threshold fluence F_{tr}, at which visible film modification occurs, we use the radius-fluence relation of a Gaussian beam outside the focus region, for which the derivation is given in the supplementary material,

$$r = \sigma(z)\sqrt{2\,\ln\left(\frac{E_{\mathrm{p}}}{2\pi F \sigma(z)^2}\right)}. \tag{11}$$

Here, r is the radial position, z is the direction of beam propagation, $\sigma(z) = \sigma_0 + \sigma_z(z - z_0)$ denotes the standard deviation of the beam profile normal to the propagation direction, σ_0 is the standard deviation at some reference point z_0 in the beam direction, and σ_z is the rate of beam divergence in the z direction. Further, F is the laser fluence of the beam and E_{p} is the pulse energy of the laser beam. By putting in a value for F, the formula yields a corresponding radius at each z position, at which this laser fluence is reached. We estimate the radii of the treated spots on the sample and plot them against the FWHM $\left(\mathrm{FWHM} = 2\sqrt{2\ln 2}\,\sigma \approx 2.36\,\sigma\right)$ and fit the radius-fluence relation formula to it, with F as a fitting parameter to gain F_{tr}.

Due to the not perfectly circular shape of the spots, the radii have been determined by calculating the area of each spot $\sqrt{A/\pi} = r$. This area has been determined by counting pixels using k-means clustering with 2 clusters to separate the pixels of the cropped image into 2 clusters, the untreated sample surface, and the darker laser spot. The error Δr has been estimated by overlaying a circle of radius r located at the centroid of the spot cluster and counting all the non-overlapping pixels in both clusters. The resulting area A_r is then equated to a ring of width $2\Delta r$ and average radius r to arrive at $\Delta r = A_r/4\pi r$.

With decreasing FWHM of the laser, the spot size on the sample first increases reaches a maximum and then decreases again. A fit of Eq. (11) yielded a threshold fluence F_{tr} of 16.5 mJ/cm^2.

Figure 7(b) is a magnified microscopic image of the laser-treated spot 16. The variation of color throughout the laser-treated region is substantial. The central area with the highest laser fluence exhibits a greenish tint, where the film has undergone considerable modification. A pinkish halo encircles this central zone, suggesting a gradient of transformation with less material modification. Also visible is the edge of the spot, which separates the spot from the unaffected area outside.

The Raman spectra in Fig. 7(c), corresponding to the locations indicated in Fig. 7(b), reveal significant changes in the laser-treated regions of the Sb_2S_3 thin film. As the line scan progressed from the edge of the spot toward the center, with the highest laser fluence, two trends emerged. First, the prominent Sb_2S_3 peaks at 280 and 300 cm^{-1} exhibited substantial broadening. Second, the silicon substrate peak at 520 cm^{-1} increased dramatically in intensity from the spot edge to the center.

A more quantitative analysis of the Raman spectra is shown in Fig. 7(d), where a linear mixture model was used to estimate the amorphous and crystalline phase fractions for each spectrum.

We assume that all the spectra s_k are a linear combination of the outermost spectrum s_{o} and the innermost spectrum s_{i},

$$s_k = \gamma_k s_{\mathrm{o}} + \zeta_k s_{\mathrm{i}}. \tag{12}$$

Ideally, the phase fractions γ_k and ζ_k add up to 1. In our analysis, this resulted naturally without enforcing it. The silicon substrate peak is visible in all spectra, which indicates that always the whole layer is probed by the laser. From simulations [Figs. 5(b) and 5(d)], we already know that the thin film melts from the top toward the substrate, so in the semi-molten regime, an amorphous layer on top of unmolten material is to be expected. In other words, the amorphous and the crystalline regions are separated across the thickness of the film, and the intensities are, therefore, additive, and this linear model can be applied.

In the first spectrum outside the treated region, the material is fully crystalline, while in the last spectrum, the material is fully amorphous, which is supported by the simulation results in Figs. 5(a)–5(c). All spectra have been used up to 450 cm^{-1} and normalized to the area under the curve, to ensure that fluctuations of the Raman intensity do not influence the resulting phase fractions and to account for the different Raman tensor elements.

From the outside to the inside of the spot, the amorphous fraction first is non-existent even near the edge of the spot where the film is visibly altered, and at 50 mJ/cm^2, it starts to rise rapidly until the increase is slowed in a way that a shoulder can be observed.

DISCUSSION

In this section, we will outline general principles, which need to be understood for the simulation and optimization of devices based on PCM thin films, with the help of our Sb_2S_3 film simulations. These will be interference, reflectivity, absorption, standing waves, melting modes, the influence of the substrate, cooling behavior, and crystallization timescales.

First, we will address the ideal thickness value of the film to achieve efficient heating. Reflectivity and the absorbed laser fluence can vary widely, depending on film thickness due to interference. In Fig. 5(a), these thickness oscillations are very visible in the average molten fraction. Heating is most effective near film thicknesses $d_{\mathrm{ar},m}$ that have an antireflective effect. At these thicknesses, the light gets partially confined inside the layer, and the absorbed energy increases as the reflection of energy is minimized for the

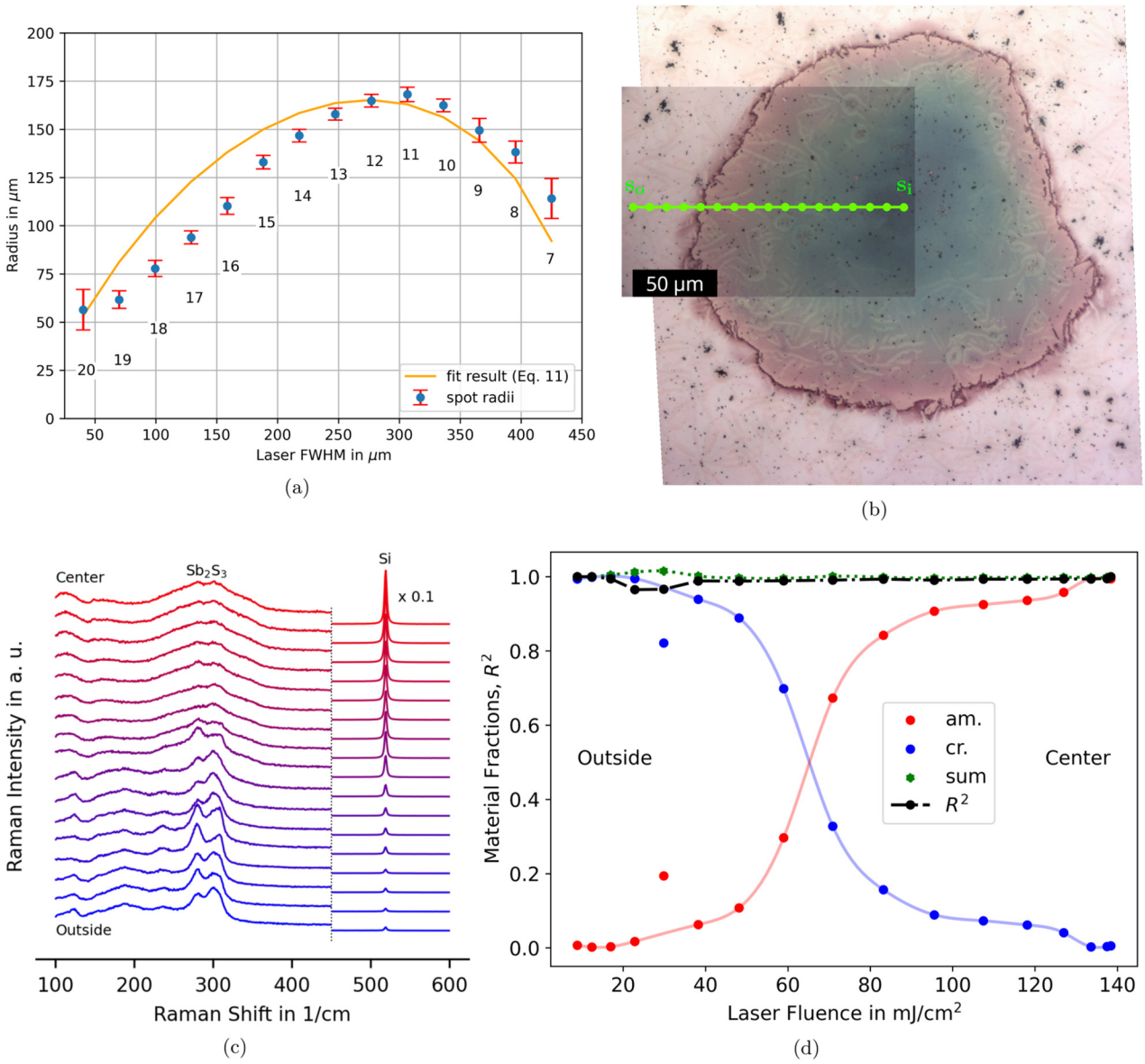

FIG. 7. (a) Radii of the visible spots in the raster vs FWHM of the laser beam with spot indices indicated. The solid curve is a fit with the threshold fluence F_{tr} as the sole fitting parameter with a fitted value of 16.5 mJ/cm^2. (b) Magnified image of spot 16 from the raster on the thin film. Insert: Region where the Raman spectra were recorded with a line scan of 17 measurement points. (c) Raman spectra from line scan across spot 16 in Fig. 7(b). The blue spectrum at the bottom is the outermost one, while the top spectrum in red was acquired at the center of the spot. (d) Estimated crystalline and amorphous fraction vs laser fluence for each Raman spectrum marked with dots, the solid lines are for guiding the eye. The fluence has been estimated using a gaussian beam profile, with the center of the beam aligned to the strongest sample change in spot 16. The coefficient of determination R^2 of the fit and the sum of the fractions are displayed. The fifth spectrum is an outlier right at the edge of the spot.

normal angle of incidence,

$$d_{\mathrm{ar},m} = \frac{(1+2m)}{4}\frac{\lambda_0}{n},\ m \in \{0, 1, 2, 3, \ldots\}. \tag{13}$$

These thicknesses provide a good initial indication; however, the absorption maxima only coincide exactly with the reflection minima for thick films and weak absorption. Thin films and strong absorption lead to a shift in the optimal thickness for heating to larger values than the antireflective thickness, especially for $m \in \{0, 1\}$, which are considered here.

In our case, the first ($m = 0$) and most pronounced heating maximum is located around a film thickness of 50 nm, which is

larger than the 35 nm for $d_{ar,0}$. The same is true for $(m = 1)$, which is around 120 nm with a $d_{ar,1}$ of 106 nm. The reflection minima and the absorption maxima shift to larger film thicknesses as the film melts progressively because the effective refractive index is decreasing and, therefore, the wavelength in the layer is increasing. The shift of the $(m = 1)$ maximum during melting is approximately three times as large as for $(m = 0)$,

$$\frac{\partial d_{ar,m}}{\partial n} = -\frac{(1+2m)}{4}\frac{\lambda_0}{n^2}. \tag{14}$$

Next, we consider the uniformity of heating and the different modes of melting in the film. Inside the thin film, the electric field will form standing waves (see Fig. 2), because the film boundaries to the air and the substrate create conditions, similar to an optical resonator at the nanoscale. These waves are more pronounced for low absorption (liquid Sb_2S_3) because standing waves are always a superposition of forward and backward traveling waves. For high absorption (crystalline Sb_2S_3), those will be dampened.

The wavelength of those waves is λ_0/n, assuming low absorption. The wavelength of the oscillations in the temperature profiles is with $\lambda_0/(2n)$ half as much, as they stem from the absorbed power. The latter is proportional to the square of the standing waves of the electric field [see Eq. (1)]. In our simulations, this can be seen in Figs. 5(b) and 5(d), with the wavelength of the temperature oscillations of 114 nm in the molten state and 71 nm in the solid state.

The position and value of the maxima of those temperature oscillations in the film are extremely important. For instance, their location in the molten state affects the film's ablation behavior. If a temperature maximum is close to the substrate, as shown in Figs. 8 and 5(d), and the evaporation threshold is reached, a large part of the entire film will be ablated. This is because evaporation will create immense pressure near the substrate, and this pressure can only be relieved by a partial lifting of the film.

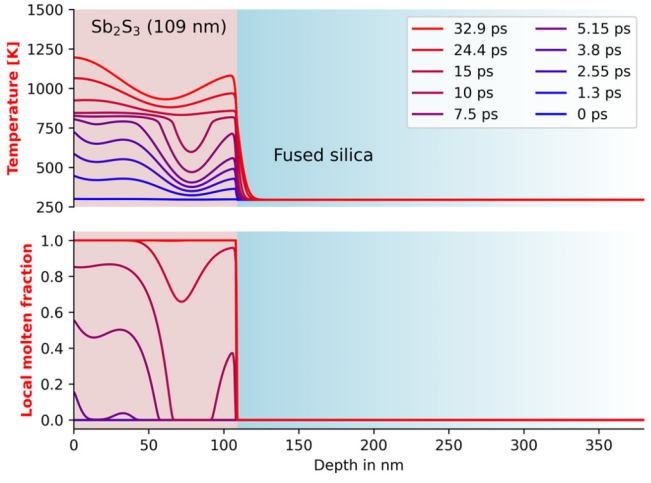

FIG. 8. Time evolution of temperature (top panel) and local molten fraction (bottom panel) within a 109 nm thick, thin film of crystalline Sb_2S_3 on a fused silica substrate during laser irradiation. The laser fluence was halved to 69 mJ/cm^2 in this simulation.

Similarly, strong oscillations in the solid state can hinder uniform melting. The melting process and its progression are entirely dependent on the locally absorbed power and how it evolves throughout the process. Melting can proceed in various ways that we will call melting modes: from the top toward the substrate [as shown in Figs. 5(b) and 5(d)], in the reverse direction, or starting from the center and moving outward. It is also possible for separate regions to melt and fuse together, as well as any combination of the mentioned melting modes (Fig. 8).

In general, heating in Sb_2S_3 slows with an increasing amount of molten material because the effective absorption of the solid-molten mixture drops with an increasing local molten fraction. Such a self-limiting heating process is a desirable property of Sb_2S_3. In other materials like GaS,[17] where the absorption in the molten state is higher than in the solid state, the material becomes unstable during optical heating, leading to early evaporation.

To enhance self-limiting heating, the film thickness should be optimized for high absorption when solid to maximize heating, and a low absorption in the liquid state to minimize heating.

The substrate also plays a crucial role and should be chosen wisely. To demonstrate the strong influence of the substrate, the simulation from Fig. 5(b) was repeated in Fig. 8 with the same parameters but with a fused silica substrate, which has a lower refractive index than Sb_2S_3. The laser fluence was reduced by half. The heating is roughly twice as efficient, achieving similar temperatures, and the highest temperature is not in the center of the film but at the surface. Notably, compared to the silicon substrate, there is now a temperature minimum near the center of the film. This is because the standing wave pattern is shifted. After all, reflection at the film/silicon interface causes a phase jump of 180° in the electric field, while reflection at the film/fused silica interface does not, as fused silica has a lower refractive index than Sb_2S_3. As a result, the melting proceeds differently with a strong dip in the local molten fraction near the center of the film. Furthermore, changing the substrate significantly slows the cooling dynamics because the thermal conductivity is two orders of magnitude lower.

Cooling plays a crucial role in the amorphization process, as shown in Fig. 5(c). The timescale of solidification is 65 ns for the film thickness of 109 nm. The cooling rate sets a hard lower limit for the amorphization time and the switching from crystalline to amorphous states.

Using the heat equation, one can show[40,41] that for a thin film, the cooling time τ_c increases quadratically as the thickness d of the film increases,

$$\tau_c \propto \frac{d^2}{a}, \quad R_c = \frac{\Delta T}{\tau_c} \propto \frac{a}{d^2}. \tag{15}$$

This results in an average cooling rate R_c during τ_c, with ΔT being the temperature difference between the start and the end of the cooling time. To achieve a high cooling rate, minimal solidification time, and rapid switching, the film should be as thin as possible. For example, the simulated solidification times of uniformly molten films with a starting temperature of 973 K with thicknesses of 77, 109, and 154 nm are 26, 47, and 93 ns, respectively.

Additionally, it is beneficial for the thin film itself to have a high thermal diffusivity. If not, at least the substrate should have a high thermal diffusivity, like silicon in our study. A popular substrate material is Si_3N_4, which has a lower thermal diffusivity than silicon, but it is still high enough that the solidification time is practically the same. More importantly, the low absorption of Si_3N_4 minimizes substrate heating, which enhances cooling. With a Sb_2S_3 thin film of 109 nm thickness, the solidification time does not increase more than 10% compared to silicon unless the thermal diffusivity of the substrate is less than 20× the thermal diffusivity of the thin film (0.15 mm^2/s).

To further enhance cooling, substrate heating can be minimized by choosing a film/substrate combination, where the light transmission to the substrate and the substrate absorption at the laser wavelength are low. In addition, short heating times are preferable to reduce substrate heating through heat conduction.

As a key advantage, these rapid simulations enable us to optimize the laser amorphization process and device performance. We construct a figure of merit η_{dev}, which captures energy efficiency, melting effectiveness, and cooling speed of the amorphization process. Additionally, we include a measure of device performance via the reflectivity contrast between the amorphous and the crystalline thin film at the application wavelength,

$$\eta_{dev} = \frac{F}{F_0} + w_1 \cdot \frac{f_s}{f_{s,0}} + w_2 \cdot \frac{d^2}{d_0^2} + w_3 \cdot \left|\frac{\Delta R_0}{\Delta R}\right|. \quad (16)$$

Here, ΔR represents the difference in reflectivity between the fully amorphous and the fully crystalline film, and F_0, $f_{s,0}$, d_0, and ΔR_0 are typical values for the system of interest for normalization, taken as 69 mJ/cm^2, 0.5, 109 nm, and 0.5, respectively. The variables w_1, w_2, and w_3 are weighting factors to make tradeoffs, if necessary, for a specific use case, but we set them to 1. By tuning the laser fluence and film thickness, we minimize η_{dev} to determine the optimal parameters, as detailed in the supplementary material. These parameters ensure that the laser energy required for melting is minimized while achieving the most complete melting possible. Furthermore, the minimization considers the need for a short cooling time [see Eq. (15)] and a high reflectivity contrast between the amorphous and crystalline states. In Fig. 9, we optimized η_{dev} to a value of 2.501. This yielded a film thickness of 58 nm and a laser fluence of 29.4 mJ/cm^2. This film thickness, slightly above the optimal thickness for heating, ensures efficient heating. Additionally, the layer thickness facilitates rapid cooling. With an average molten fraction of 0.929 at the end of the laser pulse, the film achieves near-complete melting using minimal laser fluence. Also, the reflectivity difference of 0.304 is considerable with reflectivities of 0.023 and 0.328 for the amorphous and crystalline films, respectively.

To validate our model and study laser fluence effects on thin films, we conducted experiments with varying laser fluences to determine the threshold for melting.

Figure 6(c) shows that there is some threshold fluence, which needs to be exceeded (lower row, spots 1–5 are hardly visible) to cause a modification of the thin film. As the threshold fluence is exceeded, the film melts more and more, and in the last few spots, ablation sets in. In the last spot, almost all the film is ablated,

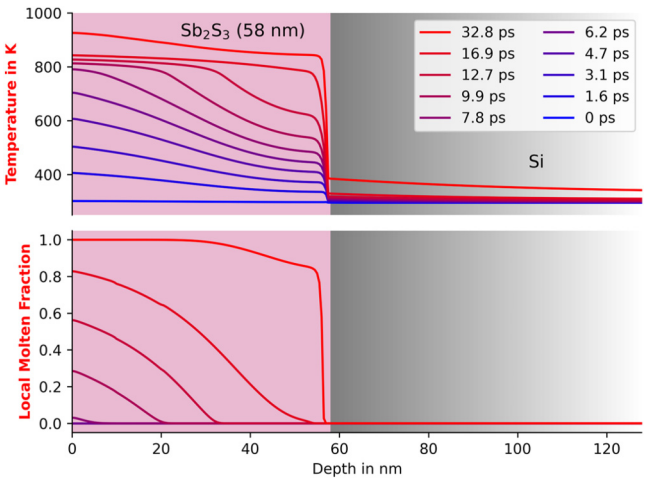

FIG. 9. Laser amorphization with optimized film thickness and laser fluence.

which was also confirmed by Raman spectroscopy and AFM. The evolution of the size of the treated area follows the trend shown in Fig. 6(b) when the beam is more and more focused.

Looking at Fig. 7(a), we determined that the threshold fluence for film modification, F_{tr}, is 16.5 mJ/cm^2, which is similar to the amorphization threshold of 20 mJ/cm^2 reported in a previous study.[21] However, it is not clear how much of the material was actually amorphized in that study, as only color changes of the sample were checked. At F_{tr}, enough of the film is molten and resolidifies in the amorphous state, such that a change can be seen in the microscopy images and, to a minor degree, in the Raman spectra.

Spot 16 in Fig. 7(b) shows that the crystal domains fade away when the laser fluence increases toward the center of the spot. This is in line with our newly found insight from the simulation in Figs. 5(b) and 5(d), which suggests that the film is progressively melting from the top toward the substrate as more laser energy enters the film.

In the Raman spectra in Fig. 7(c), we found that the intensity of the crystalline peaks diminishes progressively upon laser-induced amorphization of Sb_2S_3, while concurrently, broader amorphous peaks emerge underneath and increase in intensity. Furthermore, the silicon substrate peak is increasing when moving to the center. This increase is an indication that the film has gotten more transparent at the exciting wavelength, which is the case for the amorphous phase when compared to the crystalline phase. Also, the film could be somewhat thinner due to partial ablation, which would also enhance the silicon substrate peak.

The Raman spectra have been analyzed by using a linear mixture model to arrive at an estimate for the respective amorphous and crystalline fractions for each spectrum [Fig. 7(d)].

Before entering this discussion, we need to address recrystallization because the situation is rather complex. The most convenient model for crystallization, isothermal crystallization with homogenous nucleation does not apply in this case but is still useful for understanding. This process can be phenomenologically described

by the Avrami equation[42]

$$f_c(t, T) = 1 - \exp(-k(T) \cdot t^q) \,. \tag{17}$$

Here, f_c ranges from 0 to 1 and represents the fraction of material that has crystallized at time t. Further, $k(T)$ is the temperature-dependent rate constant that includes nucleation and growth rates, and q is the Avrami exponent, which depends on the mechanism and dimensionality of crystal growth. The rate constant and the Avrami exponent must be determined experimentally and are crucial for predicting the crystallized fraction at different temperatures and times.

After considering cooling rates and crystallization, we would like to know, under which conditions successful amorphization is possible. In general, the cooling rate must be high enough, such that there is not enough time for crystalline nuclei to form and grow. A more formal way to put this is

$$-\frac{1}{T_m - T_{end}} \overline{\frac{\partial T(t)}{\partial t}} \gg \overline{\frac{\partial f_c(T, t)}{\partial t}}. \tag{18}$$

This condition says that the averaged cooling rate $-\overline{\partial T(t)/\partial t}$ in a given temperature interval normalized to this temperature interval $T_m - T_{end}$ must exceed the averaged crystallization rate $\overline{\partial f_c(T, t)/\partial t}$ in the same temperature interval dramatically. To estimate an upper bound for the amount of recrystallization, we use established temperature-dependent parameters from the literature[43] for the Avrami model at 255–270 °C and extrapolate to the melting temperature of 550 °C of bulk Sb_2S_3. This yields a crystallized fraction of 1.4×10^{-3} after 65 ns. This naïve extrapolation suggests that the amount of crystallization may be negligible, which we assume for the further analysis of Raman spectra. This means that the average molten fraction from the simulation is the same as the amorphous fraction in the experiments, so we can compare them.

When we compare the overall shape of the curve, with the parameter map in Fig. 5(a), then the onset of melting, the rise of the amorphous fraction, and the saturation at higher laser fluence can be clearly seen. This qualitatively supports the validity of the modeling approach.

Upon comparing the enlarged view of the laser spot 16 in Fig. 7(b), one notices that the eighth/ninth spectrum counted from the edge is approximately the boundary separating the slightly altered and the fully amorphous regions. The transition is smooth, and between the eighth/ninth spectrum, 50% amorphization is crossed (Fig. 10). This location distinguishes two areas: the central region where crystal domains are no longer visible, and the annular region surrounding it, where crystal grains are still visible. In the microscope image in Fig. 7(b), the eighth/ninth spectra are the boundary between pinkish and greenish regions. The simulations and Raman spectroscopy results show reasonable qualitative agreement in terms of the onset of melting, the rise of the amorphous fraction, and the saturation at higher laser fluences (Fig. 10). However, there is a quantitative difference in the laser fluences at which 50% of the material is molten: around 20 mJ/cm^2 in the simulation vs 60 mJ/cm^2 suggested by the Raman spectra analysis. This discrepancy may be attributed to the limitations of the linear mixture model used in the Raman data analysis, which does not account for depth-dependent sampling, and the irregularity of spot 16, which might affect the estimation of laser fluences using an idealized Gaussian beam profile and analyzing a line scan.

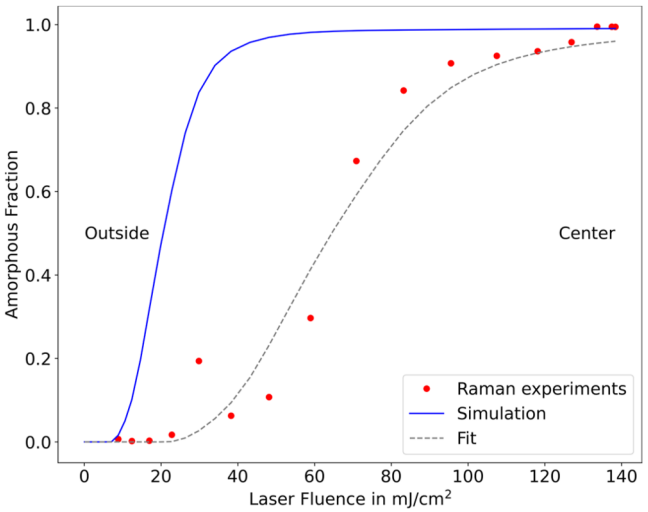

FIG. 10. Amorphous fraction vs energy density, displaying experimental data obtained through Raman spectroscopy vs the simulation model. The dashed line is an example of a least squares fit of the model to the data. For the fit, the fifth point at 30 mJ/cm^2 has been ignored.

While our current analysis provides valuable insights, we recognize the need for more advanced techniques to fully understand the laser-induced amorphization dynamics in Sb_2S_3 thin films. In an upcoming paper, we present a sophisticated analysis using imaging ellipsometry combined with holistic image analysis. Preliminary results from this analysis confirm the top-to-bottom melting process predicted by our simulations. Interestingly, the discrepancies in energy scale persist even when beam irregularities are averaged out through holistic analysis. We also considered photoluminescence as a potential explanation for the discrepancy between our simulations and experimental results. Additional spectroscopic measurements confirmed that these effects were negligible and not significant enough to account for the observed differences. This suggests that the observed differences between simulations and experiments may have a more fundamental origin.

One potential explanation for these discrepancies is saturable absorption, where phenomenologically the absorption coefficient α decreases at high laser intensities I,

$$\alpha = \alpha(I) = \frac{\alpha_0}{1 + I/I_s} \,. \tag{19}$$

Here, α_0 is the linear absorption coefficient and I_s is the saturation intensity. This happens because electrons in the ground states(s) get depleted by light absorption. Recent studies have demonstrated the saturable absorption properties of Sb_2S_3 both through direct nonlinear optical measurements[44] and by utilizing Sb_2S_3 as a saturable absorber for pulsed lasers.[45,46] Given the high

laser intensities used in our experiments (detailed absorption estimates in the supplementary material), it is highly likely that the absorption behavior of Sb_2S_3 deviates from the linear regime assumed in our current model. Saturable absorption leads to a reduction in absorption at high fluences, accounting for the higher experimental fluences required to achieve similar levels of melting compared to our simulations.

We want to compare experiments, simulations, and literature. Specifically, we look at the fluence at the midpoint of the melting interval between the completion of melting/amorphization and the onset of evaporation/ablation. Experiments from the literature[21] yield a fluence of approximately 40 mJ/cm^2 for a 93 nm thick film with a 30 nm SiO_2 capping layer using a laser with a wavelength of 532 nm, but a much longer pulse duration of 500 ps. This is less than in our experiments, which suggest a value of more than 120 mJ/cm^2, if evaporation starts after complete melting. This is due to the unclear ablation threshold as minor evaporation can go unnoticed without a capping layer. We attribute a large part of this difference to saturable absorption because in our experiments, the pulse duration is much shorter (33 ps vs 500 ps), and thus saturable absorption is much more noticeable due to higher laser intensity. Similarly, our simulations (which do not account for saturable absorption) yield a value of 85 mJ/cm^2, which is much lower than the 120+ mJ/cm^2 in our experiments.

Despite the discrepancies observed, our approach demonstrates significant value in understanding the complex dynamics of laser-induced melting in Sb_2S_3 thin films. Without our simulations, it would be impossible to know if there are unexpected physical effects like saturable absorption at play or not.

Building upon this qualitative agreement, our fast simulation model creates a unique opportunity to refine the lesser-known parameters of the model by fitting them to experimental data. This not only enhances the understanding of their impact on the experiments but also improves the accuracy of these parameter estimates. To demonstrate the flexibility of the simulations, we have included in Fig. 10, a fit to the experimental data. In this comparison, we fitted a multiplicative correction factor of 0.319 to the laser fluence to show the speed and versatility of the simulations. This factor can be viewed as a very rough account of saturable absorption, in the sense that the absorption is only 32% of the unsaturated case. A fully accurate account of saturable absorption would require an extended simulation framework due to the strong nonlinear nature of the effect. With this obtained factor and a laser fluence of 65 mJ/cm^2 needed for 50% amorphization (see Fig. 10) and a pulse duration of 33 ps, we estimate the saturation intensity I_s with 9.2×10^8 W/cm^2 using Eq. (19). Compared to the previously mentioned literature, where a pulse duration of 500 ps was used in experiments, the laser intensity in their study is lower by a factor of 33 ps/500 ps due to the longer pulse duration. Additionally, it is lower by a factor of (40 mJ/cm^2)/(120 mJ/cm^2) = 1/3, as only 40 mJ/cm^2 were needed to induce full melting in their experiments compared to our 120 mJ/cm^2. The combination of these factors yields an overall factor of 0.022. With that, the saturation of absorption is minimal with 500 ps pulses as the absorption is at 95.5% of the unsaturated value. Comparing the two percentages yields with 95.5%/31.9% a theoretical factor of 2.99. So, in our experiment, three times as much laser fluence would be needed to fully melt the film when compared to the experiments with 500 ps laser pulses, which is roughly the case: 120+ mJ/cm^2 in our experiments vs 40 mJ/cm^2 in the literature.

However, our modeling provides crucial insights into the laser-induced amorphization dynamics of phase-change materials, and there are several avenues for future research and modeling improvements. The most salient would be the investigation of saturable absorption. Experimentally, we suggest varying the pulse duration of the laser to change the intensity and, therefore, the strength of the saturation of the absorption. We suggest experiments with a pulse duration of 100 ps or longer to compare with simulations, which can be done with our code. To directly study saturable absorption in Sb_2S_3 films, much shorter pulse durations like 3 ps or even in the femtosecond range would be also very enlightening. Measuring with a femtosecond pulse would allow us to study saturable absorption without melting the thin film.

One further area of focus is modeling the recrystallization process, which presents unique challenges and opportunities for further investigation. In our case, during cooling, the temperature changes and, therefore, non-isothermal generalizations of the Avrami equation [Eq. (17)], which lead to nonlinear integral equations[47] are needed. Furthermore, the spatially inhomogeneous distribution of unmolten crystal grains in the semi-molten regime requires going beyond homogenous nucleation. To fully capture this complexity of the amorphous-to-crystalline transition in such cases, phase field models[48,49] need to be employed and extended.

In addition to these experimental and modeling advancements, the use of complementary characterization techniques like imaging ellipsometry and electron microscopy can provide important experimental data for further in-depth analysis, enabling extra refinement of the simulation framework.

CONCLUSION

We have developed a comprehensive simulation framework to model laser-induced amorphization dynamics in phase-change material (PCM) thin films, incorporating critical factors, such as thin film interference, heat transfer, and melting-induced change of optical properties. This framework provides a more complete and accurate representation of the complex processes involved compared to existing models. Simulations reveal the significant role of interference in determining absorbed laser energy distribution and melting dynamics.

For Sb_2S_3 films, we constructed a wide-ranging high-resolution parameter map of melting behavior vs laser fluence and film thickness. Experimental picosecond laser amorphization validates simulation trends, with Raman spectroscopy confirming the polycrystalline-to-amorphous transition and providing qualitative agreement with predictions. The discrepancies between simulations and Raman analysis are a strong hint to the occurrence of saturable absorption.

Nevertheless, overall trends are consistent, supporting the modeling approach. The computational speed of our framework enables not only the investigation but also the optimization of the amorphization process and the device performance. This is achieved by tuning film thickness and laser parameters to maximize energy efficiency, melting effectiveness, and quenching rate as

well as the reflectivity contrast for any PCM thin film system. Also, parameter fitting in conjunction with experimental data is possible.

This powerful, experimentally validated simulation framework provides fundamental insights into Sb_2S_3 laser amorphization dynamics. More broadly, it opens new avenues for simulation-guided optimization of PCMs and thin film stacks for demanding photonic applications. Future work will focus on advanced experiments and simulations to quantify the effect of saturable absorption and to extract key parameters, refine models, and extend to other promising PCMs, accelerating the development of novel, high-performance phase-change photonic devices.

SUPPLEMENTARY MATERIAL

The supplementary material document provides details on the simulation methodology, fitting and optimization methods, mathematical relations for estimating laser fluence, and the absorbed number of photons.

ACKNOWLEDGMENTS

The authors acknowledge support from the European Union's Horizon 2020 research and innovation program (No. 899598—PHEMTRONICS), the Ramon y Cajal Fellowship (No. RYC2022-037828-I) from the Ministerio de Ciencia, Innovación y Universidades (MCIU), and the Danube Project (Project No. MULT 07/2023) from the OeAD-GmbH (OEAD).

AUTHOR DECLARATIONS

Conflict of Interest

The authors have no conflicts to disclose.

Author Contributions

J. Resl: Conceptualization (equal); Data curation (lead); Formal analysis (lead); Investigation (lead); Methodology (equal); Resources (supporting); Software (lead); Validation (equal); Visualization (lead); Writing – original draft (lead); Writing – review & editing (equal). **K. Hingerl:** Conceptualization (equal); Funding acquisition (equal); Methodology (supporting); Project administration (supporting); Resources (lead); Supervision (equal); Validation (supporting); Writing – review & editing (equal). **Y. Gutierrez:** Funding acquisition (supporting); Project administration (supporting); Visualization (supporting); Writing – review & editing (equal). **M. Losurdo:** Conceptualization (supporting); Funding acquisition (lead); Project administration (lead); Resources (supporting); Writing – review & editing (equal). **C. Cobet:** Conceptualization (equal); Formal analysis (supporting); Funding acquisition (supporting); Investigation (supporting); Methodology (lead); Project administration (supporting); Resources (equal); Supervision (equal); Validation (equal); Visualization (supporting); Writing – review & editing (equal).

DATA AVAILABILITY

The data that support the findings of this study are available within the article. The code for the simulations is available in GitHub, Ref. 25.

REFERENCES

[1]Y. Saito, M. Morota, K. Makino, J. Tominaga, A. V. Kolobov, and P. Fons, Mater. Sci. Semicond. Process. **135**, 106079 (2021).
[2]P. Moitra, Y. Wang, X. Liang, L. Lu, A. Poh, T. W. W. Mass, R. E. Simpson, A. I. Kuznetsov, and R. Paniagua-Dominguez, Adv. Mater. **35**, e2205367 (2023).
[3]G. Chen, J. Zhou, S. E. Bopp, J. Zhao, and Z. Liu, Opt. Lett. **47**, 4040 (2022).
[4]G. Santos, M. Losurdo, F. Moreno, and Y. Gutiérrez, Nanomaterials (Basel, Switzerland) **13**, 496 (2023).
[5]L. Lu, Z. Dong, F. Tijiptoharsono, R. J. H. Ng, H. Wang, S. D. Rezaei, Y. Wang, H. S. Leong, P. C. Lim, J. K. W. Yang, and R. E. Simpson, ACS Nano **15**, 19722 (2021).
[6]G. Santos, M. Georghe, C. Cobianu, M. Modreanu, M. Losurdo, Y. Gutiérrez, and F. Moreno, Opt. Express **30**, 38953 (2022).
[7]K. Zhao, J. Yang, M. Zhong, Q. Gao, Y. Wang, X. Wang, W. Shen, C. Hu, K. Wang, G. Shen, M. Li, J. Wang, W. Hu, and Z. Wei, Adv. Funct. Mater. **31**, 2006601 (2021).
[8]D. Pérez-Francés, G. Santos, J. Resl, M. Losurdo, Y. Gutiérrez, and F. Moreno, Opt. Mater. Express **13**, 3677 (2023).
[9]P. Hosseini, C. D. Wright, and H. Bhaskaran, Nature **511**, 206 (2014).
[10]W. Chen, S. Liu, and J. Zhu, Int. J. Extreme Manuf. **6**, 35501 (2024).
[11]J. Feldmann, N. Youngblood, M. Karpov, H. Gehring, X. Li, M. Stappers, M. L. Gallo, X. Fu, A. Lukashchuk, A. S. Raja, J. Liu, C. D. Wright, A. Sebastian, T. J. Kippenberg, W. H. P. Pernice, and H. Bhaskaran, Nature **589**, 52 (2021).
[12]C. Ríos, M. Stegmaier, P. Hosseini, D. Wang, T. Scherer, C. D. Wright, H. Bhaskaran, and W. H. P. Pernice, Nat. Photonics **9**, 725 (2015).
[13]Y. Gutiérrez, A. P. Ovvyan, G. Santos, D. Juan, S. A. Rosales, J. Junquera, P. García-Fernández, S. Dicorato, M. M. Giangregorio, E. Dilonardo, F. Palumbo, M. Modreanu, J. Resl, O. Ishchenko, G. Garry, T. Jonuzi, M. Georghe, C. Cobianu, K. Hingerl, C. Cobet, F. Moreno, W. H. P. Pernice, and M. Losurdo, iScience **25**, 104377 (2022).
[14]M. Delaney, I. Zeimpekis, D. Lawson, D. W. Hewak, and O. L. Muskens, Adv. Funct. Mater. **30**, 2002447 (2020).
[15]W. Dong, H. Liu, J. K. Behera, L. Lu, R. J. H. Ng, K. V. Sreekanth, X. Zhou, J. K. W. Yang, and R. E. Simpson, Adv. Funct. Mater. **29**, 1806181 (2019).
[16]Y. Zhou, K. Huang, L. Zhou, X. Cheng, M. Xu, H. Tong, and X. Miao, RSC Adv. **9**, 9457 (2019).
[17]Y. Gutiérrez, S. Dicorato, A. P. Ovvyan, F. Brückerhoff-Plückelmann, J. Resl, M. M. Giangregorio, K. Hingerl, C. Cobet, M. Schiek, M. Duwe, P. H. Thiesen, W. H. P. Pernice, and M. Losurdo, Adv. Opt. Mater. **12**, 2301564 (2024).
[18]U. Chalapathi, B. Poornaprakash, C.-H. Ahn, and S.-H. Park, Appl. Surf. Sci. **451**, 272 (2018).
[19]Y. Gutiérrez, S. Espinoza, M. Zahradník, K. Khakurel, J. Resl, C. Cobet, K. Hingerl, M. Duwe, P. Thiesen, and M. Losurdo, Thin Solid Films **763**, 139580 (2022).
[20]R. J. Appleton, Z. D. McClure, D. P. Adams, and A. Strachan, J. Chem. Phys. **160**, 174702 (2024).
[21]C. Laprais, C. Zrounba, J. Bouvier, N. Blanchard, M. Bugnet, A. Gassenq, Y. Gutiérrez, S. Vazquez-Miranda, S. Espinoza, P. Thiesen, R. Bourrellier, A. Benamrouche, N. Baboux, G. Saint-Girons, L. Berguiga, and S. Cueff, Adv. Opt. Mater. **12**, 2401214 (2024).
[22]R. A. Ghez and R. A. Laff, J. Appl. Phys. **46**, 2103 (1975).
[23]S. B. Mansoor and B. S. Yilbas, Opt. Quantum Electron. **42**, 601 (2011).
[24]N.-H. Cheung, J. Appl. Phys. **70**, 7654 (1991).
[25]J. Resl, GitHub Repository (2024), see https://github.com/city-ships/pulsewise.
[26]Z. Fang, J. Zheng, A. Saxena, J. Whitehead, Y. Chen, and A. Majumdar, Adv. Opt. Mater. **9**, 2002049 (2021).
[27]L. Lu, S. F. G. Reniers, Y. Wang, Y. Jiao, and R. E. Simpson, J. Opt. **24**, 94001 (2022).
[28]S. Sadasivam, M. K. Y. Chan, and P. Darancet, Phys. Rev. Lett. **119**, 136602 (2017).
[29]P. Lautenschlager, M. Garriga, L. Vina, and M. Cardona, Phys. Rev. B **36**, 4821 (1987).

[30]H. R. Shanks, P. D. Maycock, P. H. Sidles, and G. C. Danielson, Phys. Rev. **130**, 1743 (1963).
[31]F. Abelès, J. Phys. Rad. **11**, 307 (1950).
[32]M. V. Klein and T. E. Furtak, *Optik* (Springer XV, Berlin, 1988).
[33]D. A. G. Bruggeman, Ann. Phys. **416**, 636 (1935).
[34]G. K. Johnson, G. Papatheodorou, and C. E. Johnson, J. Chem. Thermodyn. **13**, 745 (1981).
[35]K. Aryana, H. J. Kim, M. R. Islam, N. Hong, C.-C. Popescu, S. Makarem, T. Gu, J. Hu, and P. E. Hopkins, Opt. Mater. Express **13**, 3277 (2023).
[36]GESTIS-Stoffdatenbank, (2024), see https://gestis.dguv.de/data?name=004590.
[37]J. A. Woollam Company, "CompleteEASE software" (2022), available at https://www.jawoollam.com/ellipsometry-software/completeease.
[38]J. Resl, Y. Gutiérrez, and M. Losurdo (2023), "Database of New Phase Change Materials," Zenodo.
[39]M. T. S. Nair, Y. Peña, J. Campos, V. M. García, and P. K. Nair, J. Electrochem. Soc. **145**, 2113 (1998).
[40]J. Fourier, *Théorie Analytique de la Chaleur* (Didot, 1822).
[41]E. Buckingham, Phys. Rev. **4**, 345 (1914).
[42]M. Avrami, J. Chem. Phys. **7**, 1103 (1939).
[43]A. Taute, S. Al-Jibouri, C. Laprais, S. Monfray, J. Lumeau, A. Moreau, X. Letartre, N. Baboux, G. Saint-Girons, L. Berguiga, and S. Cueff, Opt. Mater. Express **13**, 3113 (2023).
[44]C. Wu, C. Zhao, L. Wang, Z. Xie, Z. Wang, and S. Zhou, ACS Appl. Nano Mater. **4**, 13425 (2021).
[45]X. Yao, Y. Liu, S. Liu, Q. Zhang, and G. Hu, Opt. Fiber Technol. **82**, 103616 (2024).
[46]Q. Hu, X. Chen, M. Li, P. Li, L. Xu, H. Zhao, B. Zhang, J. Liu, and K. Yang, Molecules (Basel, Switzerland) **27**, 745 (2022).
[47]V. Erukhimovitch and J. Baram, J. Non-Cryst. Solids **208**, 288 (1996).
[48]J. Berry and M. Grant, Phys. Rev. E **89**, 62303 (2014).
[49]M. Vasin and V. Ankudinov, Math. Methods Appl. Sci. **47**, 6798-6809 (2024).